Macromolecules

ARTICLE

pubs.acs.org/Macromolecules

Primitive Chain Network Simulation of Elongational Flows of Entangled Linear Chains: Role of Finite Chain Extensibility

Takatoshi Yaoita,[†,‡,⊥] Takeharu Isaki,[‡] Yuichi Masubuchi,[†] Hiroshi Watanabe,[†,*] Giovanni Ianniruberto,[§] and Giuseppe Marrucci[§]

[†]Institute for Chemical Research, Kyoto University, Kyoto 611-0011, Japan

[‡]Material Science Laboratory, Mitsui Chemicals Inc., Chiba 299-0265, Japan

[§]Dipartimento di Ingegneria Chimica, Università "Federico II", P. le Tecchio 80, 80125 Napoli, Italy

ABSTRACT: For entangled linear monodisperse polymers, uniaxial elongational flow behavior was examined with the primitive chain network (PCN) simulation, which was originally formulated for a network of Gaussian chains bound by sliplinks but was modified in this study to properly take into account the finite extensibility of actual chains. On an increase of the elongational rate $\dot{\varepsilon}$ from the terminal relaxation frequency $1/\tau_d$ (at equilibrium) to the Rouse relaxation frequency $1/\tau_R$, the original and modified simulations gave an indistinguishable steady state elongational viscosity η_E that almost scaled as $\dot{\varepsilon}^{-1/2}$. On a further increase of $\dot{\varepsilon} > 1/\tau_R$, η_E obtained from the original PCN simulation diverged to infinity (as noted also for the unentangled Rouse chains). In contrast, η_E deduced from the modified simulation increased but did not diverge with increasing $\dot{\varepsilon} > 1/\tau_R$ (similarly to the behavior of FENE dumbbells). This feature of the modified PCN simulation, i.e., hardening to a finite (nondiverging) level, mimicked the η_E data of entangled semidilute solutions, which naturally reflected the finite extensibility of actual chains. Analysis of the simulation results suggested that the power law behavior ($\eta_E \sim \dot{\varepsilon}^{-1/2}$) at $1/\tau_d < \dot{\varepsilon} < 1/\tau_R$ is related to reduction of the entanglement density and the corresponding reduction of chain tension, while the hardening (upturn of η_E at $\dot{\varepsilon} > 1/\tau_R$) results from stretch of the chain (eventually approaching full stretch), thus shedding light on the behavior of semidilute solutions. Nevertheless, the modified simulation did not describe the behavior of entangled melts, i.e., $\eta_E \sim \dot{\varepsilon}^{-1/2}$ even at $\dot{\varepsilon} > 1/\tau_R$. A factor missing in the modified simulation is discussed in an attempt to elucidate, from a molecular point of view, the difference between entangled solutions and melts.

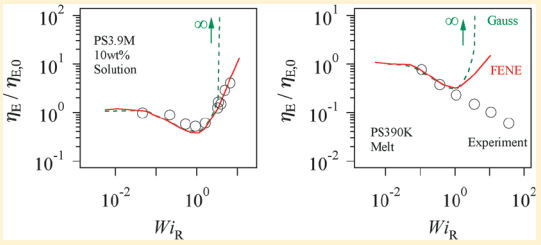

1. INTRODUCTION

For entangled polymers, extensive studies have been made experimentally and theoretically to elucidate, from a molecular viewpoint, the role of entanglements. In particular, the tube model refined so as to include a variety of molecular relaxation mechanisms helped us to understand entangled polymer dynamics to a considerable depth.[1−4] Nevertheless, several important experimental observations have not been fully addressed within the context of the refined tube model and remain as subjects of theoretical challenge.

One of the current challenges, a major one, relates to the uniaxial elongational flow behavior of entangled monodisperse linear chains. Figure 1 schematically illustrates the strain rate ($\dot{\varepsilon}$) dependence of the steady state elongational viscosity (η_E) of monodisperse linear polystyrene (PS) reported in the extensive work by Sridhar's group (for entangled semidilute solutions)[5−7] and by Hassager's group (for entangled melts).[8,9] With increasing $\dot{\varepsilon}$ from the reciprocal of the terminal relaxation time τ_d at equilibrium (often interpreted as the reptation time) to the reciprocal of the Rouse relaxation time τ_R of the whole chain, η_E of both solutions and melts decreases, essentially scaling as $\eta_E \propto \dot{\varepsilon}^{-1/2}$. However, on a further increase of $\dot{\varepsilon} > 1/\tau_R$, η_E of the entangled solutions increases (without diverging) to a level even above the linear-regime viscosity $\eta_{E,0}$ (= $3\eta_0$), whereas η_E of the entangled PS melts does not show this hardening behavior but keeps decreasing roughly as $\eta_E \propto \dot{\varepsilon}^{-1/2}$.

Here we rely on the experimental data mentioned above, although PS melt data from a different laboratory[10] also confirm Hassager's data. As regards possible differences between solution and melt experiments, we recall that both data sets were taken by the filament stretching rheometer with similar feedback systems to achieve constant elongational rates. Some minor differences may exist in sample adhesion to the end-plates and in thermal equilibration, but such aspects certainly cannot explain the marked differences in rheological behavior schematically reported in Figure 1.

Theoretical attempts have been made for explaining this difference of the elongational flow behavior of entangled solutions and melts. For example, the tube model refined by Mead, Larson, and Doi (MLD)[11] accounting for the nonequilibrium mechanism of convective constraint release (CCR),[12] and the resulting dynamic tube dilation (DTD),[13] can mimic the η_E data of the entangled solutions, as reported by Sridhar and co-workers.[5−7] However, the η_E data of the entangled melts do not appear to be consistently explained by the MLD model

Received: September 26, 2011
Revised: November 13, 2011
Published: December 01, 2011

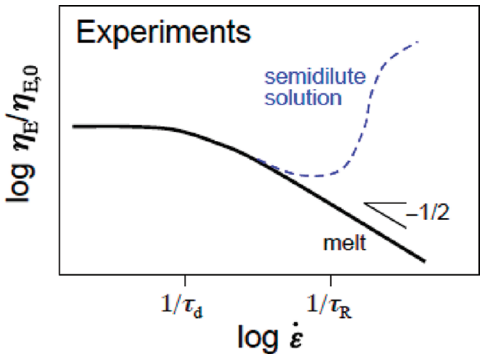

Figure 1. Schematic illustration of uniaxial steady-state elongational viscosity η_E of entangled melts and semidilute solutions of monodisperse linear chains. $\eta_{E,0}$ is the steady-state viscosity in the linear range.

even after a reasonable change of the model parameters. Wagner and co-workers[9] incorporated the concepts of interchain pressure (ICP) due to tube confinement and of strain-dependent tube diameter[14,15] in their molecular stress function model and showed that the η_E data of the melts can be described by this model. Nevertheless, the tube diameter relaxation time required for description of the data has not been fully explained within the context of the model, and remains as an adjustable parameter. In addition, incorporation of both CCR and ICP effects in the tube model could result in underestimation of the η_E data of the melts,[16] despite the fact that CCR is an unavoidable ingredient of the tube model under flow.

It should be noted that the extensional behavior of dilute solutions has been extensively studied as well.[17−22] For example, Gupta et al.[21] have reported that some dilute and semidilute (unentangled) solutions also show the $\eta_E \propto \dot{\varepsilon}^{-1/2}$ behavior in the range of $\dot{\varepsilon} > 10/\tau_R$. This behavior has been explained by the chain finite extensibility[20] and by the friction anisotropy.[18,21] However, it is well-known that the molecular mechanisms relevant for entangled solutions and melts are very much different from those prevailing in dilute solutions.[1,4]

In view of the above recalled uncertainties, this paper analyzes the many-chain dynamics under elongational flow with the aid of the primitive chain network (PCN) simulation[23] (i.e., by replacing the *tube confinement* with binary sliplinks). The PCN simulation successfully described the linear viscoelastic and nonlinear shear thinning behavior[23−27] as well as the nonlinear damping behavior[28] of entangled linear chains. In the simulations with the *original* PCN code,[23−26,28] the entangled system was modeled as a network of *Gaussian* chains bound by sliplinks, and these chains were allowed to move/relax through reptation/contour length Rouse fluctuation through the sliplinks,[1] as well as through CCR[12] and thermal CR[29] induced by removal and creation of sliplinks. In this study on *uniaxial* elongational flows, we used a *modified* PCN code that accounts for finite extensibility, as also done by Shaqfeh and co-workers in their multichain sliplink model when examining the nonlinear behavior under shear[30] and *planar*[31] extensional flows.

More specifically, in this study we first conducted the PCN simulation with the original *Gaussian* code under uniaxial elongational flow conditions in the expectation that the calculated η_E decreases essentially as $\dot{\varepsilon}^{-1/2}$ for $1/\tau_d < \dot{\varepsilon} < 1/\tau_R$ (as found also from the single chain sliplink model by Schieber and co-workers[32]) but diverges at $\dot{\varepsilon} > 1/\tau_R$ because of the infinite extensibility of Gaussian chains. Since actual chains have an extension limit,[30,31] we then incorporated finite extensibility in the PCN code, with the expectation that this modification would allow the simulation to predict the hardening but nondiverging η_E thus mimicking the data of the entangled solutions schematically shown in Figure 1. We do not expect, however, that the modified simulation successfully describes the melt data, and we will discuss possible factors distinguishing melts from solutions, postponing a detailed analysis of such factors to a subsequent paper.

2. MODEL

In the PCN simulation,[23−28] sliplinks are distributed along the polymer chains to divide them into subchains having a molecular weight comparable to the entanglement molecular weight. Each sliplink bonds two chains, consistently with the binary assumption for entanglements. The sliplink is allowed to move in space according to a balance among drag force, subchain tensions, osmotic force, and random thermal force. The polymer chain slides through the sliplinks (i.e., reptates) to fulfill the force balance along the chain. If the end of the chain moves past a sliplink, that sliplink is removed. On the contrary, if the monomers (taken to be the Kuhn segments) reptate, by a certain amount, beyond the sliplink located at the chain end, a new sliplink is created by hooking one of the surrounding chains. In summary, dynamics of the system is ruled by: 3D motion of the sliplinks, monomer reallocation between adjacent subchains via chain sliding through the sliplinks, and creation/removal of sliplinks at chain ends. The above dynamics is described by the stochastic equations summarized below, with the finite extensibility of the chains (not considered in the original Gaussian PCN code) affecting the equations for sliplink position and monomer number per subchain through the expression for the elastic force.

2.1. 3D Motion of Sliplinks. The sliplink position, $\mathbf{R}$, obeys the time-evolution equation representing the force balance mentioned above:[23]

$$\zeta(\dot{\mathbf{R}} - \boldsymbol{\kappa}\mathbf{R}) = \mathbf{F}_B + \mathbf{F}_f + \sum_i^4 \mathbf{F}_i \quad (1)$$

Here, $\dot{\mathbf{R}}$ is the time derivative of $\mathbf{R}$, and $\boldsymbol{\kappa}$ the velocity gradient tensor. $\mathbf{F}_B$ is the thermal random force, $\mathbf{F}_f$ the osmotic force due to concentration fluctuation of the sliplinks, and $\mathbf{F}_i$ the elastic force in the i-th subchain of the 4 subchains acting upon the sliplink of our focus. The friction coefficient ζ of the sliplink is assumed to be given by

$$\zeta = 4\frac{n_0}{2}\zeta_m \quad (2)$$

where n_0 is the average number of monomers (Kuhn segments) in the subchain at equilibrium, and ζ_m is the monomeric friction coefficient. The factor of 4 accounts for the number of subchains converging to the sliplink, while the factor $^1/_2$ reflects the fact that the subchain friction is split into the two sliplinks confining the subchain.

Among the forces appearing in eq 1, $\mathbf{F}_B$ is modeled as a white noise having zero mean and the second-order moment given by,[23]

$$\langle \mathbf{F}_B(t)\mathbf{F}_B(t')\rangle = 2kT\zeta\delta(t-t')\mathbf{I} \quad (\mathbf{I} = \text{unit tensor}) \quad (3)$$

with kT being the thermal energy. $\mathbf{F}_f$ is related to the chemical potential μ as $\mathbf{F}_f = -\nabla\mu$. The free energy A, giving

μ as a derivative, is of the simple form:

$$A = \begin{cases} \varepsilon\left(\dfrac{\phi}{\langle\phi\rangle} - 1\right)^2 & \text{for} \quad \phi > \langle\phi\rangle \\ 0 & \text{for} \quad \phi \le \langle\phi\rangle \end{cases} \tag{4}$$

In eq 4, ϕ is the local subchain density (number of subchains in the entanglement volume $a^3 = (b(n_0)^{1/2})^3$, with b = Kuhn length), $\langle\phi\rangle$ is the average of ϕ in the whole system, and ε is a numerical factor specifying the magnitude of $\mathbf{F}_f$ (ε = 0.5, following a previous study[25]).

Finally, $\mathbf{F}_i$ is the elastic force of the i-th subchain acting on the sliplink[27]

$$\mathbf{F}_i = f\frac{3kT}{n_i b^2}\mathbf{r}_i \tag{5}$$

with $\mathbf{r}_i$ being the end-to-end vector and n_i the monomer number of the i-th subchain. If the subchain is treated as the infinitely extensible Gaussian chain (as in the original PCN code[23]), the factor f appearing in eq 5 is given by

$$f = 1 \tag{6}$$

On the other hand, for the actual subchains with the finite extensibility, f can be expressed within the FENE-P approximation as[33]

$$f = \frac{1}{1 - \langle(r_i/r_{i,\max})^2\rangle_i} \quad \text{with } r_i = |\mathbf{r}_i| \tag{7}$$

Here, $r_{i,\max}$ (= bn_i) is the fully stretched i-th subchain length. The use of FENE-P rather than FENE eliminates numerical difficulties due to overstretched segments artificially generated by Brownian kicks and/or conformational rearrangements upon creation of sliplinks. Obviously, the difference between eqs 6 and 7 has a significant effect on the PCN simulation results only when the subchains are considerably stretched.

In relation to eq 7, we should point out that in a previous work[27] we used the PCN model with FENE rather than FENE-P. The use of FENE requires several changes in the constraint renewal algorithm (to be explained in section 2.3) and such changes induce differences in the basic parameters (units of length and time[27]) as well as in chain statistics.[34] Since we have confirmed that, in spite of those differences, the rheological responses predicted by the PCN-FENE and PCN-FENE-P codes are similar to one another, for simplicity we use here the FENE-P approximation.

2.2. 1D monomer reallocation through sliplinks. Subchain monomers are redistributed as a result of differences of tensions of adjacent subchains, of chemical potential gradients along the chain, and of one-dimensional Gaussian random force. The rate of sliding of monomers ($\dot{n}$) from the (i−1)-th to the i-th subchain through the sliplink is described by:

$$\zeta_s\frac{\dot{n}}{\rho} = (F_i - F_{i-1}) + f_B + f_f \tag{8}$$

In eq 8, ρ is the linear density of monomers averaged over the (i−1)-th and the i-th subchains, and ζ_s is the friction coefficient for the sliding motion, simply computed by taking half the (equilibrium) monomers in each subchain:

$$\zeta_s = 2\frac{n_0}{2}\zeta_m = n_0\zeta_m \tag{9}$$

The elastic tension F_i appearing in eq 8 is related to r_i and to the factor f defined by eqs 6 and 7 (without/with the finite extensibility) through the scalar equivalent of eq 5:

$$F_i = f\frac{3kT}{n_i b^2}r_i \tag{10}$$

The other force appearing in eq 8, f_f, is the scalar equivalent of $\mathbf{F}_f$, i.e., the field force along the chain due to fluctuations in subchain density.[23] Finally, f_B is the 1D Brownian force characterized by:

$$\langle f_B(t) f_B(t')\rangle = 2kT\zeta_s\delta(t - t') \tag{11}$$

Recently Uneyama and Masubuchi[35] have proposed a modification of the monomer sliding equation, eq 8, for better thermodynamic consistency (use of chemical potential differences instead of tension balance). However, extension of this modification to fast flows appears nontrivial, and therefore we here stick for simplicity to the standard PCN code to focus on the effect of finite extensibility.

2.3. Constraint Renewal. Each chain creates and destroys sliplinks at its ends, thus renewing the topology of the entangled network (constraint renewal). In the simulation, creation and/or destruction of sliplinks results from monitoring the monomer number in the end subchains. The end subchain creates a new entanglement when its monomer number exceeds $1.5n_0$, while it removes its entanglement when the monomer number falls below $0.5n_0$.[24] Although this algorithm is clearly somewhat arbitrary, and its relationship to thermodynamics (detailed balance) remains unclear, it recommends itself for its simplicity and for its good performance in reproducing both linear[24−26,34] and nonlinear[26,28] rheology of linear polymers.

2.4. Simulations. In the simulation, the Langevin equations, eqs 1 and 8, were solved numerically to follow the time evolution of $\{\mathbf{R}_i\}$, $\{\mathbf{r}_i\}$, and $\{n_i\}$ and to calculate the stress tensor $\boldsymbol{\sigma}$,

$$\boldsymbol{\sigma} = \frac{1}{V}\sum_i \mathbf{F}_i\mathbf{r}_i - p\mathbf{I} = \frac{1}{V}\frac{3kT}{b^2}f\sum_i \frac{\mathbf{r}_i\mathbf{r}_i}{n_i} - p\mathbf{I} \tag{12}$$

Here, the sum extends over all subchains in the volume V, f is the FENE factor defined by eqs 6 and 7, and p is the isotropic pressure (that balances the chain stress components perpendicular to the elongational direction). In the actual simulation, eqs 1 and 8 were nondimensionalized with the aid of the units of length, thermal energy, and time, $a = b(n_0)^{1/2}$, kT, and $\tau_0 = n_0^2 b^2\zeta_m/3kT$, respectively. (Consequently, $\boldsymbol{\sigma}$ was obtained in the nondimensionalized form.)

The simulation conditions, such as the number density of subchains per unit volume and the periodic boundary condition, are the same as in our previous work.[23] A simulation box with dimensions of 8 × 8 × 8 was used for calculations of linear viscoelasticity. For uniaxial deformation, a flat simulation box 4 × 104 × 104, with 4 in the stretching direction, was used as the starting box, and the simulation was stopped either when a steady flow was achieved or when the box elongational ratio Λ reached the maximum value $\Lambda_{\max}$ = 676 (*i.e.*, when the deformed box became 2704 × 4 × 4) corresponding to an Hencky strain ($\varepsilon_H = \ln\Lambda$) of ca. 6.5. The simulation box size did not affect the results, as explained in Appendix A.

Equilibration of the starting box was achieved by simulation under quiescent conditions for a sufficiently long time (longer than the longest relaxation time of the system). For a chain with molecular weight M, the number of subchains per chain is given by $Z_0 = M/M_0$, with M_0 being the average molecular weight of the

subchains. The average monomer number per subchain, n_0, was calculated from the Kuhn molar mass M_{Kuhn} as $n_0 = M_0/M_{Kuhn}$.[23] The length of the fully stretched subchain is given by $r_{i,max} = bn_i$ and its nondimensional expression is related to n_0 as $\tilde{r}_{i,max} = bn_i/b(n_0)^{1/2} = n_i/(n_0)^{1/2}$.

The parameters required for the nondimensional simulation are Z_0 and n_0. From the modulus $G_0 = \rho RT/M_0$ we obtain M_0, hence Z_0 from M. Finally n_0 is obtained from M_{Kuhn}. Comparison of the nondimensional simulation results with data also requires the unit of time τ_0. The parameters G_0 and τ_0 were unequivocally evaluated by fitting the linear viscoelastic data with the PCN simulation (under no strain), as explained in Appendix B.

3. RESULTS AND DISCUSSION

3.1. Overview of Data and Simulation Results. In Figure 2, symbols show the data of the viscosity growth function $\eta_E^+(t,\dot{\varepsilon})$ reported for a polystyrene (PS) solution ($M = 3.9 \times 10^6$, c = 10 wt %)[6] and a PS melt ($M = 3.9 \times 10^5$).[8] The curves indicate

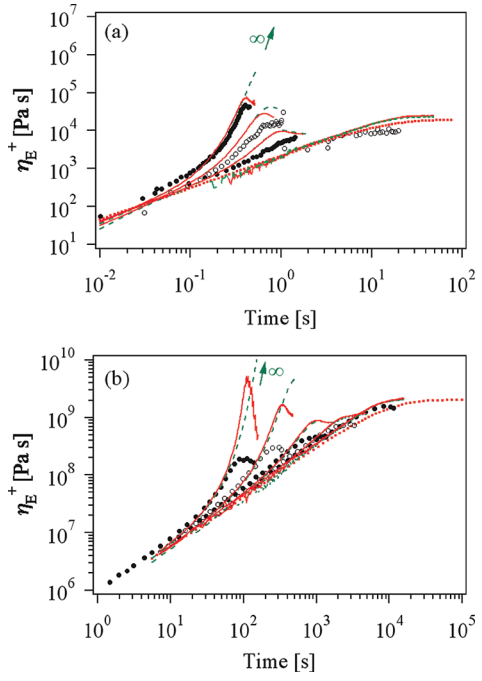

Figure 2. Transient uniaxial viscosity $\eta_E^+(t,\dot{\varepsilon})$ for (a) solutions and (b) melts of monodisperse linear polystyrene (PS). Experimental data for the solution (symbols) are obtained from ref. 6: $M = 3.9 \times 10^6$, c = 10 wt %, T = 21 °C, and $\dot{\varepsilon}$ = 0.1, 3.5, 7.3, and 11.7 s^{-1}. Experimental data for the melt (symbols) are obtained from ref. 8: $M = 3.9 \times 10^5$, T = 130 °C, and $\dot{\varepsilon}$ = 0.0003, 0.001, 0.003, 0.01, and 0.03 s^{-1}. Simulation results with and without FENE are indicated with the solid and dashed curves, respectively. Thin dotted curve indicates $\eta_E^+(t)$ in the linear viscoelastic regime.

the PCN simulation results with (solid curves) and without (dashed curves) FENE. The simulation parameters, determined from the fitting of the linear viscoelastic data (cf. Appendix B), are listed in Table 1. Figures 3 and 4, respectively, show the corresponding steady state elongational viscosity, $\eta_E(\dot{\varepsilon}) = \eta_E^+(\infty,\dot{\varepsilon})$, of the solution and melt. Both the measured (symbols) and simulated (curves) viscosities are plotted against the Weissenberg number defined with respect to the Rouse relaxation time τ_R:

$$Wi_R = \tau_R\dot{\varepsilon} \quad \text{with} \quad \tau_R = \frac{Z_0^2}{2\pi^2}\tau_0 \tag{13}$$

(The Rouse time τ_R calculated from eq 13[27] is also reported in Table 1.)

As noted in Figure 2, the $\eta_E^+(t,\dot{\varepsilon})$ data of both the solution and the melt fall above the linear $\eta_E^+(t,0)$ data shown in Figure 2 with

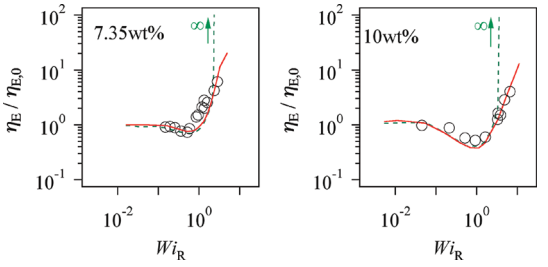

Figure 3. Steady-state uniaxial viscosity η_E for monodisperse linear PS solutions with $M = 3.9 \times 10^6$ and c = 7.35 wt % (left panel) and 10 wt % (right panel) at 21°C. The η_E data are normalized by the zero-strain-rate viscosity, $\eta_{E,0}$, and plotted against τ_R-based Weissenberg number Wi_R. The data obtained from ref. 5 are shown with the circles. Simulation results with and without FENE are indicated with the solid and dashed curves. Arrows indicate divergence for the Gaussian chain at $Wi_R \gg 1$ deduced from the simulation without FENE.

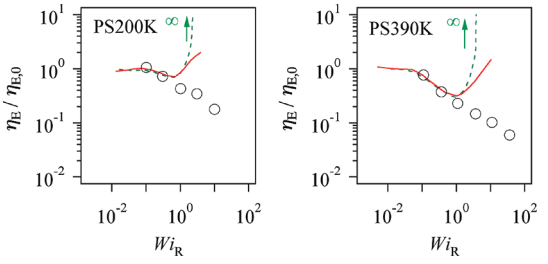

Figure 4. Steady-state uniaxial viscosityη_E for monodisperse linear PS melts with $M = 2.0 \times 10^5$ (PS200 K, left panel) and $M = 3.9 \times 10^5$ (PS390 K; right panel) at 130°C. The η_E data are normalized by the zero-strain-rate viscosity, $\eta_{E,0}$, and plotted against τ_R-based Weissenberg number Wi_R. Experimental data obtained from ref. 8 are indicated with the circles. Simulation results with and without FENE are indicated with the solid and dashed curves. Arrows indicate divergence for the Gaussian chain at $Wi_R \gg 1$ deduced from the simulation without FENE.

Table 1. Parameters of PS Samples (Solutions[5,6] and Melts[8]) Used in the Simulations

sample	M_w	Z_0	n_0	G_0 [Pa]	τ_0 [s]	τ_R [s]
3.9 M 7.35 wt % sol.	3.9×10^6	18	300	8.1×10^2	1.7×10^{-2}	2.7×10^{-1}
3.9 M 10 wt % sol.	3.9×10^6	33	160	2.0×10^3	8.3×10^{-3}	4.6×10^{-1}
PS200 K	2.0×10^5	18	15	2.9×10^5	5.6 (7.0)[a]	9.1×10^1 (1.1×10^2)[a]
PS390 K	3.9×10^5	35	15	2.9×10^5	5.6 (7.0)[a]	3.5×10^2 (4.3×10^2)[a]

[a] FENE for melts.

dx.doi.org/10.1021/ma202166y |Macromolecules 2011, 44, 9675–9682

the thin dotted curves ($=3\eta^+(t)$ obtained from the linear viscoelastic response reported in Appendix B) at short to intermediate times. This transient hardening behavior is commonly observed for solutions and melts at $Wi_R > 1$ ($\dot{\varepsilon} > 1/\tau_R$). However, in the steady extensional state, the solution and the melt of Figure 2 exhibit a significant difference: η_E ($\dot{\varepsilon}$) of the solution (Figure 3) exhibits an upturn (steady state hardening) and increases with increasing Wi_R in the range $Wi_R > 1$, while η_E ($\dot{\varepsilon}$) of the melt (Figure 4) keeps decreasing with increasing Wi_R even at such high Wi_R (roughly as $Wi_R^{-1/2}$, i.e., as $\dot{\varepsilon}^{-1/2}$).

Figure 2a demonstrates that the transient strain-hardening behavior of the solution is described by the simulation either with or without the finite chain extensibility (with eq 7 or eq 6). However, the behavior of the steady state η_E ($\dot{\varepsilon}$) data (thinning followed by the hardening without divergence) can be mimicked only when the finite extensibility is incorporated in the simulation (cf. Figure 3). This conclusion is fully confirmed by the subchain stretch obtained from the simulation, reported in Figure 5a as the reduced stretch ratio $\tilde{\lambda} = \lambda/\lambda_{max} = \langle r_i/r_{i,max}\rangle_i$. In the early stage in the transient zone, the subchains in the solution are far from the fully stretched limit ($\tilde{\lambda}$ is well below unity) so that the simulated $\eta_E^+(t,\dot{\varepsilon})$ is not significantly affected by the finite extensibility. However, in the steady flow state at large Wi_R ($\gg$1), the simulation without the finite extensibility allows the subchains to be infinitely stretched to give the diverging η_E ($\dot{\varepsilon}$). (This diverging feature is well-known for the Gaussian chain modeled as a Rouse chain.) In contrast, the simulation accounting for the finite extensibility of the actual chains can reproduce semiquantitatively both thinning and nondiverging hardening of the $\eta_E(\dot{\varepsilon})$ data (cf. Figures 2a and 3). Considering this success of the simulation with the finite extensibility, the simulated crossover from the thinning to the hardening zone is analyzed in the next section to discuss the similar crossover observed for the solutions. (Note that the PCN simulation with the original code was made also for the nonlinear stress relaxation under step strain[28] but the chain stretch under the conditions examined was well below the fully stretched limit. Thus, the results of those simulations are not affected by the FENE correction.)

Differently from solutions, the transient strain hardening of the melt is followed by the thinning of η_E ($\dot{\varepsilon}$) $\propto\dot{\varepsilon}^{-1/2}$ even at $Wi_R \gg 1$ (cf. Figures 2b and 4). This thinning at large Wi_R cannot be described by the simulation either with or without the finite extensibility, although the thinning at Wi_R of order unity appears to be better mimicked if the finite extensibility is incorporated in the simulation. Indeed, the simulations do not distinguish between melts and solutions, as also shown by the behavior of $\tilde{\lambda}$ in Figure 5 where the melt and the solution are very similar. It so appears that some essential physical factor distinguishing entangled solutions and melts is missing in the current PCN simulation. Possible physical factors responsible for this difference are discussed in the last section.

As mentioned in the Introduction, finite extensibility had already been implemented in earlier sliplink models, and used in extensional flow simulations.[27,31,32] In particular, the single-chain sliplink model of Schieber et al.[32] reproduces the $\eta_E \propto \dot{\varepsilon}^{-1/2}$ behavior in the range of $\dot{\varepsilon} > 1/\tau_R$ for melts (though departing considerably from data in the transient behavior), yet a behavior similar to melts is predicted for solutions as well, thus strongly underpredicting the solution elongational thickening. Kushwaha and Shaqfeh[31] performed

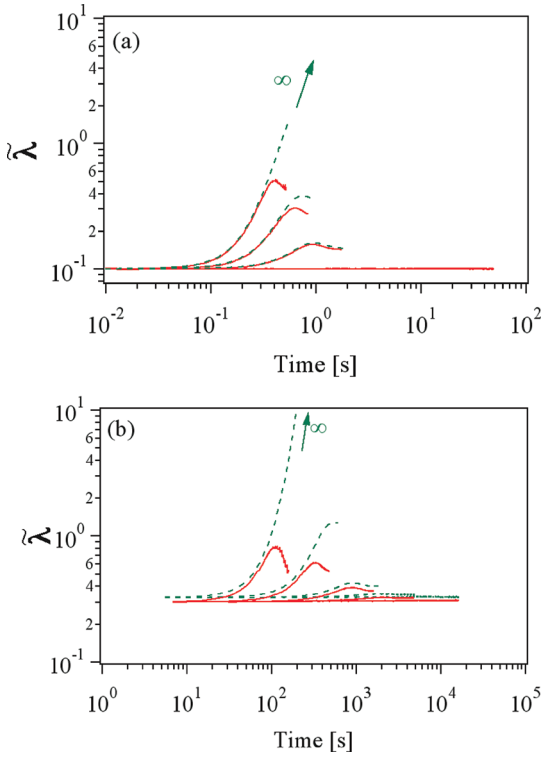

Figure 5. Simulation results for the transient stretch ratio λ normalized to λ_{max} (fully stretched subchain) corresponding to the viscosity results shown in Figure 2. (a) PS solution with $M = 3.9 \times 10^6$ and $c =$ 10 wt % at $\varepsilon = 0.1$, 3.5, 7.3, and 11.7 s^{-1} from right to left. (b) PS melt with $M = 3.9 \times 10^5$ (PS390 K) at $\varepsilon = 0.0003$, 0.001, 0.003, 0.01, and 0.03 s^{-1} from right to left. Results with and without FENE are shown with the solid and dashed curves, respectively. Arrows indicate divergence for the Gaussian chain at $Wi_R \gg 1$ deduced from the simulation without FENE.

multichain sliplink simulations under *planar* elongational flow and compared their results with melt data,[8] observing power laws similar to $\eta_E \propto \dot{\varepsilon}^{-1/2}$ in the nonlinear range, and an upturn in the viscosity only at $\dot{\varepsilon} \gg 1/\tau_R$. Although the authors[31] do not explicitly compare their predictions with entangled solution data, a "delayed" upturn is certainly in contrast with solution data in *uniaxial* elongational flow. To our knowledge, the present paper demonstrates for the first time a quantitative agreement of sliplink simulations with uniaxial extensional viscosity data of entangled solutions, showing at the same time the limitation of the current PCN code for dealing with entangled melts in uniaxial elongational flow.

3.2. Origin of Thinning Followed by Nondiverging Hardening of Solutions. Since the PCN simulation with FENE mimicked the elongational behavior of entangled solutions, analysis of the simulation results allows us to examine the factors responsible for the thinning-thickening crossover of the solution. We start from the expression of the stress tensor $\boldsymbol{\sigma}$ (cf. eq 12 with eq 7 for FENE), where for convenience of this analysis we adopt a decoupling approximation, and express the reduced tensile stress σ_E^{rd} as

$$\sigma_E^{rd} \equiv \frac{1}{\nu kTZ_0}(\sigma_{xx} - \sigma_{yy}) \cong 3f\lambda^2 S\left(\frac{Z}{Z_0}\right) \tag{14}$$

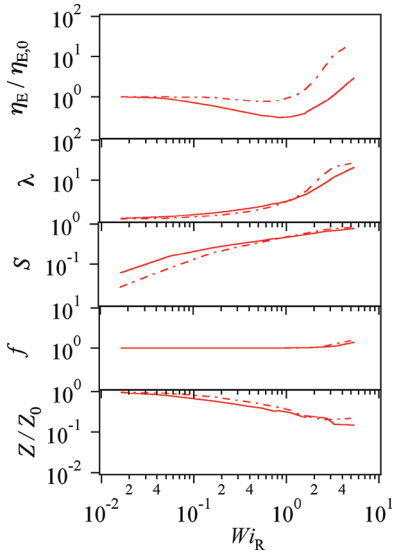

Figure 6. Average stretch ratio λ, orientation anisotropy S, FENE factor f, and reduced entanglement density Z/Z_0 obtained from the PCN-FENE simulation for the entangled solutions (dashed and solid curves for c = 7.35 and 10 wt %, respectively) in the steady flow state as a function of Wi_R. For comparison, the simulated viscosity η_E is also shown (topmost panel).

where ν is the (constant) number of chains per unit volume, and Z/Z_0 as well as

$$\lambda = \left\langle \frac{r_i^2}{n_i b^2} \right\rangle_i^{1/2}, \quad S = \left\langle \frac{(\mathbf{r}_i\mathbf{r}_i)_{xx} - (\mathbf{r}_i\mathbf{r}_i)_{yy}}{|\mathbf{r}_i|^2} \right\rangle_i,$$
$$f = \frac{1}{1 - \langle (r_i/r_{i\max})^2 \rangle_i} \tag{15}$$

are quantities variable with the stretching rate.

In Figure 6, the average stretch ratio λ, the orientation anisotropy S, the FENE factor f, and the reduced entanglement density Z/Z_0, all obtained from the PCN-FENE simulation for the entangled solutions in the steady flow state, are plotted against Wi_R. For comparison, the simulated viscosity η_E is also shown.

Figure 6 shows that, in the range $Wi_R < 1$, both λ and S increase whereas Z/Z_0 decreases with increasing Wi_R, and f remains close to unity. Now, since the viscosity η_E is given by $\eta_E \sigma_E/\dot{\varepsilon} = \sigma_E \tau_R/Wi_R$, the decrease of Z/Z_0 significantly adds to the decreasing factor $1/Wi_R$ in overwhelming the increase of S (enhancement of orientation) and λ (enhancement of stretch) to give the thinning behavior of η_E. Thus, the thinning behavior is attributable, to a significant extent, to the CCR mechanism that results in the decrease of the entanglement density Z/Z_0 and in the corresponding reduction of the chain tension, the latter being given by the product of three factors, i.e., $\lambda f Z/Z_0$. In contrast, in the range of $Wi_R > 1$, λ and f increase more rapidly with increasing Wi_R while the decrease of Z/Z_0 remains similar to that in the range $Wi_R < 1$. Thus, the hardening of η_E seen at $Wi_R > 1$ is governed by enhancement of the chain tension due to chain stretching toward the fully stretched limit. (The orientation S tends to saturate at such large Wi_R and has virtually no effect on the hardening.)

3.4. Possible Origin of Lack of Hardening of Melts. As shown in the previous sections, the behavior of entangled solutions, i.e., thinning of η_E followed by thickening, is well captured by the PCN simulation incorporating reptation, contour length fluctuations, thermal CR and CCR, and the FENE correction. Hence, the lack of hardening observed for entangled PS melts (Figure 3b) is quite possibly due to some extra factor other than those listed above.

Some years ago an extra factor was proposed, related to the tube constraint and called interchain pressure (ICP),[14] which generated the prediction $\eta_E \propto \dot{\varepsilon}^{-1/2}$ under steady, moderately fast, elongational flows. Later, tube models somehow incorporating ICP[9] predicted monotonic thinning of η_E ($\propto \dot{\varepsilon}^{-1/2}$) even in very fast flows, i.e., at $Wi_R > 1$, in agreement with the observed behavior of PS melts. However, combination of ICP and CCR, the latter being an essential ingredient in the tube model, results in excessive thinning stronger than the observation.[16] In addition, there is no conceptual reason why the ICP effect should be active only in melts and not in entangled solutions where the constraining tube is also present.

A possible candidate factor discriminating between entangled melts and entangled solutions is the anisotropic change of the friction coefficient tensor under strong flows. An anisotropic friction was proposed long ago by Giesekus,[36] and further developed by Wiest.[18] Their constitutive equations, incorporating the anisotropic friction for a dumbbell model, show that the steady elongational viscosity can decrease for $Wi_R > 1$. Gupta et al.[21] showed that the constitutive equation by Wiest reasonably reproduces the extensional viscosity of dilute polymer solutions. However Wiest equation cannot be used for the case of entangled polymers because of the separate role played by Wi and Wi_R, where Wi controls orientation of the entangled subchains while Wi_R determines subchain stretch.[1] For the case of entangled polymers, the flow-induced anisotropic reduction of the monomeric friction has recently been reconsidered by Ianniruberto and co-workers[37] and later by Uneyama and co-workers[38] in their rheo-dielectric analysis. Within the context of a flow-induced frictional anisotropy, the difference between entangled melts and solutions might arise from the fact that, in a monodisperse melt, each stretched and oriented subchain is surrounded by similarly stretched/oriented material, whereas in entangled solutions subchains are surrounded by solvent molecules that remain isotropic under all conditions. We are now attempting to evaluate the magnitude of the friction reduction from experimental data available in the literature so as to use the outcome in the PCN simulation without introducing any additional parameter. The results will be reported in a subsequent paper.

4. CONCLUDING REMARKS

We have implemented finite extensibility (FENE) into the original PCN code to investigate the behavior of both transient and steady-state viscosity (η_E) under fast uniaxial elongation of entangled polymers. The PCN simulation with the FENE effect well mimicked the behavior of the entangled semidilute solutions, i.e., the thinning of η_E at extensional rates $\dot{\varepsilon}$ between τ_d^{-1} and τ_R^{-1} then followed by nondivergent thickening at $\dot{\varepsilon} > \tau_R^{-1}$. In the range $\tau_d^{-1} < \dot{\varepsilon} < \tau_R^{-1}$, where finite extensibility is not yet important, the simulation revealed an important contribution of the CCR mechanism to the thinning behavior of the steady-state elongational viscosity, resulting in a decrease of the entanglement density with increasing $\dot{\varepsilon}$, and the corresponding reduction of the chain tension. Conversely, for $\dot{\varepsilon} > \tau_R^{-1}$, the simulation shows that the thickening results from the enhancement of chain tension due to chain stretching toward the fully stretched limit.

These simulation features provide us with a clue for better understanding the elongational thinning/thickening behavior of entangled semidilute solutions.

However, the PCN-FENE simulation cannot describe the behavior of entangled PS melts, i.e., monotonic thinning of η_E observed even at $\dot{\varepsilon} > \tau_R^{-1}$. Thus, this monotonic thinning must be attributed to an extra mechanism not considered in the current PCN-FENE simulation. The stretch/orientation-dependent frictional anisotropy might be the factor that gives rise to monotonic thinning in fast extensional flows of entangled melts. Incorporation of the latter mechanism in the PCN-FENE simulation is now being attempted, and the results will be reported in a subsequent paper.

APPENDIX A. EFFECT OF SIMULATION BOX SIZE

We have checked the effect of simulation box size to verify possible artifacts due to periodic boundary conditions. Figure 7 shows the time development of the (nondimensional) elongational viscosity for the longest chains examined in the paper (Z_0 = 35), at Wi_R = 0.35 and Wi_R = 3.5, for various box dimensions. The simulation was always halted when the box dimension became equal to 4 in the directions normal to the uniaxial stretch. Figure 7a reports results obtained with several rectangular cuboid (flat) boxes having the same initial dimension in the stretching direction (set to 4) but different dimensions in the direction orthogonal to the stretch. In order to check for possible artifacts due to the use of flat initial boxes, we also performed simulations starting with cubic boxes of various sizes, and the corresponding results are shown in Figure 7b. Clearly, results are insensitive to both size and shape of the initial box. We used the largest box (with dimension 4 × 104 × 104) to examine the behavior in the steady flow state over a sufficiently long time.

APPENDIX B. DETERMINATION OF SIMULATION PARAMETERS

The parameters for the melt were essentially common to our earlier studies. The subchain molecular weight M_0 for PS melts has been reported earlier[25] as 1.1 × 10^4. (Notice that the value of the molar mass between consecutive sliplinks is somewhat smaller than the entanglement molar mass M_e reported in the literature.[24,25]) Using such a value, the subchain number Z_0 was determined as $Z_0 = M/M_0$ (M = molar mass of the examined melts). The unit modulus G_0 was evaluated as $G_0 = \rho RT/M_0$, with ρ and R being the density and gas constant, respectively. The unit time τ_0 has been determined earlier[25] as 2.0 × 10^{-3} s at 180 °C, and the unit time at 130 °C, τ_0 = 5.6 s, was obtained from the WLF relationship reported in ref 25. The Rouse relaxation time τ_R was determined from eq 13. The newly introduced parameter in this study is the Kuhn length $b = a/\sqrt{n_0}$ in eq 7 for the FENE effect. We determined n_0 from the molar mass of the PS Kuhn segment reported as 720.[4] As the value of n_0 comes out relatively small (n_0 = 15), a small FENE effect is present also in linear viscoelasticity. Hence a correction was necessary for the time constant τ_0. The correction was made by fitting $G^*(\omega)$, and we obtained τ_0 = 7.0 s at 130 °C.

We determined the parameters for the solutions from the data reported in ref. 5. where the concentration dependence of the entanglement molecular weight M_e was discussed in detail. Assuming that the ratio of the unit molecular weight M_0 to M_e is insensitive to the concentration (and thus the ratio is common with the melt; M_0/M_e = 1.10/1.33), M_0 for the solutions were determined from M_e at each concentration reported in ref 5.

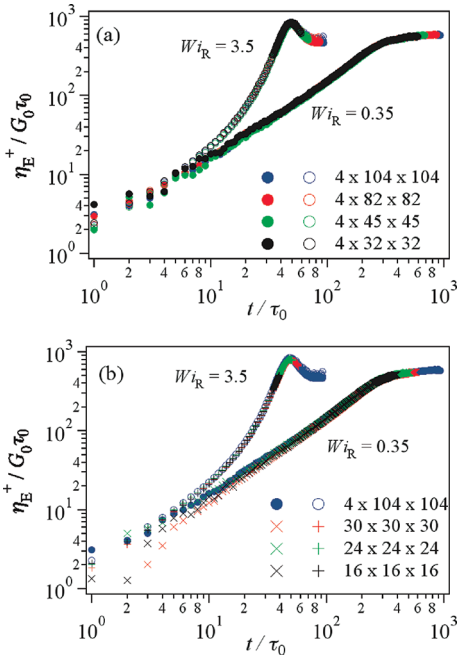

Figure 7. Transient uniaxial viscosity for chains with Z_0 = 35 at Wi_R = 3.5 and Wi_R = 0.35 obtained from simulations starting with various box dimensions. The simulations were started with (a) flat and (b) cubic boxes with the dimensions shown in the figure.

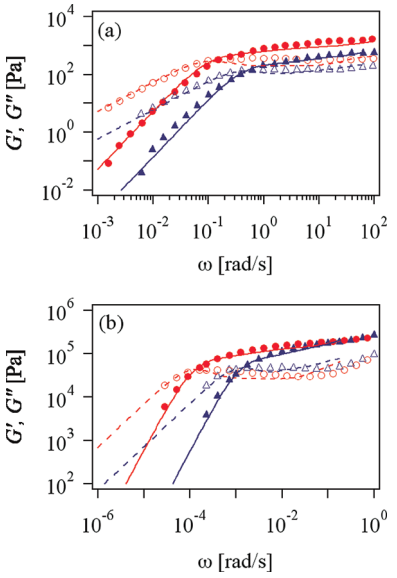

Figure 8. Linear viscoelastic G' and G'' data of (a) PS solutions with M = 3.9 × 10^6 and c = 7.35 wt % (triangles) and c = 10 wt % (circles) from ref 5 and (b) PS melts with M = 2.0 × 10^5 (triangles) and M = 3.9 × 10^5 (circles) from ref 8. Simulation results are indicated with curves.

Then Z_0, G_0 and n_0 were determined in a manner similar to that for melt. The unit time τ_0 was obtained by fitting $G^*(\omega)$ for each solution, and τ_R was calculated from Z_0 and τ_0. Since n_0 values for the solutions are sufficiently large, the FENE correction for the time constant performed for the melt case was actually not necessary.

The parameters thus obtained are summarized in Table 1. The moduli simulated with those parameters (also accounting for FENE) are shown in Figure 8 (curves). For both solutions and melts (top and bottom panels), the simulated results agree with data (symbols) reasonably well, which lends support to the parameter values used in the simulation.

AUTHOR INFORMATION

Corresponding Author

*E-mail: hiroshi@scl.kyoto-u.ac.jp.

Present Addresses

[⊥]Fabricated Products Developments Division, Mitsui Chemicals Inc., Chiba 299-0265, Japan.

REFERENCES

(1) Doi, M.; Edwards, S. *The Theory of Polymer Dynamics*, Oxford University Press: Oxford, U.K., 1986.
(2) Watanabe, H. *Prog. Polym. Sci.* **1999**, *24*, 1253.
(3) McLeish, T. C. B. *Adv. Phys.* **2002**, *51*, 1379.
(4) Rubinstein, M.; Colby, R. *Polymer Physics*: Oxford: New York, 2003.
(5) Bhattacharjee, P. K.; Oberhauser, J. P.; McKinley, G. H.; Leal, L. G.; Sridhar, T. *Macromolecules* **2002**, *35*, 10131.
(6) Bhattacharjee, P. K.; Nguyen, D. A.; Mckinley, G. H.; Sridhar, T. *J. Rheol.* **2003**, *47*, 269.
(7) Ye, X.; Sridhar, T. *Macromolecules* **2005**, *38*, 3442.
(8) Bach, A.; Almdal, K.; Rasmussen, H. K.; Hassager, O. *Macromolecules* **2003**, *36*, 5174.
(9) Wagner, M. H.; Kheirandish, S.; Hassager, O. *J. Rheol.* **2005**, *49*, 1317.
(10) Luap, C.; Müller, C.; Schweizer, T.; Venerus, D. C. *Rheol. Acta* **2005**, *45*, 83.
(11) Mead, D. W.; Larson, R. G.; Doi, M. *Macromolecules* **1998**, *31*, 7895.
(12) Ianniruberto, G.; Marrucci, G. *J. Non-Newtonian Fluid Mech.* **1996**, *65*, 241.
(13) Marrucci, G. *Polym. Sci. Polym. Phys. Ed.* **1985**, *23*, 159.
(14) Marrucci, G.; Ianniruberto, G. *Macromolecules* **2004**, *37*, 3934.
(15) Marrucci, G.; Ianniruberto, G. *J. Non-Newtonian Fluid Mech.* **2005**, *128*, 42.
(16) Dhole, S.; Leygue, A.; Bailly, C.; Keunings, R. *J. Non-Newtonian Fluid Mech.* **2009**, *161*, 10.
(17) Jones, D. M.; Walters, K.; Williams, P. R. *Rheol. Acta* **1987**, *26*, 20.
(18) Wiest, J. M. *Rheol. Acta* **1989**, *28*, 4.
(19) Quinzani, L. M.; Armstrong, R. C.; Brown, R. A. *J. Rheol.* **1995**, *39*, 1201.
(20) Li, X.; Denn, M. M. *J. Rheol.* **2004**, *48*, 805.
(21) Gupta, R. K.; Nguyen, D. A.; Sridhar, T. *Phys. Fluids* **2000**, *12*, 1296.
(22) Haward, S. J.; Sharma, V.; Odell, J. A. *Soft Matter* **2011**, *7*, 9908.
(23) Masubuchi, Y.; Takimoto, J.-I.; Koyama, K.; Ianniruberto, G.; Greco, F.; Marrucci, G. *J. Chem. Phys* . **2001**, *115*, 4387.
(24) Masubuchi, Y.; Ianniruberto, G.; Marrucci, G.; Greco, F. *J. Chem. Phys.* **2003**, *119*, 6925.
(25) Masubuchi, Y.; Ianniruberto, G.; Greco, F.; Marrucci, G. *J. Non-Newtonian Fluid Mech.* **2008**, *149*, 87.
(26) Masubuchi, Y. *Nihon Reoroji Gakkaishi (J. Soc. Rheol. Jpn.)* **2006**, *34*, 275.
(27) Yaoita, T.; Isaki, T.; Masubuchi, Y.; Watanabe, H.; Ianniruberto, G.; Greco, F.; Marrucci, G. *J. Chem. Phys.* **2008**, *128*, 154901.
(28) Furuichi, H.; Nonomura, C.; Masubuchi, Y.; Watanabe, H. *J. Chem. Phys.* **2010**, *133*, 374902.
(29) Graessley, W. W. *Adv. Polym. Sci.* **1982**, *47*, 67–117.
(30) Dambal, A.; Kushwaha, A.; Shaqfeh, E. *Macromolecules* **2009**, *42*, 7168.
(31) Kushwaha, A.; Shaqfeh, E. *J. Rheol.* **2011**, *55*, 463.
(32) Schieber, J. D.; Nair, D. M.; Kitkrailard, T. *J. Rheol.* **2007**, *51*, 1111.
(33) Peterlin, A. *J. Chem. Phys.* **1960**, *36*, 1799.
(34) Masubuchi, Y.; Uneyama, T.; Watanabe, H.; Ianniruberto, G.; Marrucci, G.; Greco, F. *J. Chem. Phys.* **2010**, *133*, 134902.
(35) Uneyama, T.; Masubuchi, Y. *J. Chem. Phys.* **2011**, *135*, 184904.
(36) Giesekus, H. *J Non-Newtonian Fluid Mech.* **1982**, *11*, 69.
(37) Ianniruberto, G.; Brasiello, A.; Marrucci, G. *Proc. 7th Annu. Eur. Rheol. Conf.* **2011**, 61.
(38) Uneyama, T.; Horio, K.; Watanabe, H. *Phys. Rev. E* **2011**, *83*, 001800.